PAPER

Check for updates

Effect of copper doping on the electrochemical behavior of SnS$_2$ electrodes for aqueous Al-ion hybrid supercapacitors†

Debayan Chatterjee [ID] ‡*[a] and Sonali Das [ID] ‡[b]

The choice and optimization of electrode materials are crucial for maximizing the energy density and optimizing the overall performance of supercapacitors. Layered metal dichalcogenides (LMDs), such as SnS$_2$, are promising faradaic materials for hybrid supercapacitors due to their layered structures and abundant sites for effective charge transport. However, their performance is often limited by low electrical conductivity and poor stability owing to low ionic transport and high volumetric expansion. This study presents a straightforward method for enhancing the performance of SnS$_2$-based electrodes by doping with copper through a facile solid-state synthesis. The incorporation of copper doping significantly improved the specific capacitance, demonstrating a near 40% increase compared to pristine SnS$_2$ without any complicated optimization procedures or the need to form any composites/heterostructures. The maximum specific capacitance achieved at a current density of 1 A g^{-1} is 98 F g^{-1} for pristine SnS$_2$ and 140 F g^{-1} for 5% Cu-doped SnS$_2$ in aqueous 1 M AlCl$_3$ electrolyte that highlights the potential of copper-doped SnS$_2$ as a high-performance electrode material for aqueous Al-ion supercapacitors, paving the way for further optimization and development of efficient and sustainable energy storage devices.

Sustainability spotlight

We know that a broad scope of science encompasses the study of energy generation, conversion and utilization, of which energy storage is a pivotal part. Our study presents a simple, eco-friendly method for enhancing SnS$_2$ supercapacitor performance through copper doping, achieving significant gains in specific capacitance and stability. The energy storage solution using a non-toxic material such as SnS$_2$ significantly aims to reduce the carbon footprint of the world and aligns with the UN's Sustainable Development Goal 7 by promoting affordable and clean energy solutions. Our findings demonstrate that straightforward material modifications can lead to high-performance energy storage devices without the need for complex, resource-intensive processes, thereby contributing to a more sustainable and cleaner future that we all aspire to for the sake of life and humanity.

1 Introduction

The scientific and technological development for energy generation and, correspondingly, storage has increased manyfolds with advancing innovations in the realm of energy storage devices. The imperative role of energy storage devices is essential in accounting for the heterogeneity in energy demand and counterbalancing the intermittency of renewable energy sources.[1,2] Energy storage technology comprises a versatile class of devices classified based on their size scale and the form in which energy is stored.[3] One of the most enormous achievements in the energy sector was the advent of supercapacitors (SCs) or ultracapacitors. After the introduction of the first SC based on RuO$_2$ by Conway in the late 1970s,[4] SCs have emerged as one of the most impactful devices in the recent years owing to their game-changing applications from an industrial perspective. SCs are devices similar in construction to most batteries, but they store energy by adsorption of solvated ions on electrodes to form an electric double layer as wide as a few nanometres. Commercial supercapacitors have low energy density ($\sim$1 to 10 W h kg^{-1}), compared to that of typical lithium ion batteries (LIBs) ($\sim$100 to 300 W h kg^{-1}) in gravimetric terms but also possess typical power densities a few order of magnitudes higher than the latter,[5,6] essentially bridging the gap between traditional capacitors and batteries (Table 1).

Over the years, material selection for the electrodes of SCs has been critical for harnessing the highest performance out of

[a]*School of Nano Science and Technology (SNST), Indian Institute of Technology, Kharagpur, India. E-mail: debayan.ch.24@kgpian.iitkgp.ac.in; debayan.7.dc@gmail.com; Tel: +91 9874-789-233*

[b]*Advanced Technology Development Centre (ATDC), Indian Institute of Technology, Kharagpur, India. E-mail: sonali.das.24@kgpian.iitkgp.ac.in; sonalidas1303@gmail.com*

† Electronic supplementary information (ESI) available. See DOI: https://doi.org/10.1039/d4su00435c

‡ These authors contributed equally to this work.

Table 1 Typical values of performance parameters of electrochemical energy storage devices

Device	Energy density (W h kg^{-1})	Power density (W kg^{-1})	References
Conventional capacitors	0.01–0.3	$\sim$10^6	7
Supercapacitors	1–20	3000–40 000	5
Lithium-ion batteries	100–300	100–1000	5

the device, be they carbon-based porous materials for electric double layer capacitors (EDLCs)[4,8] or faradaic materials for pseudocapacitors[9,10] and hybrid SCs,[11] which incorporate both the mechanisms of EDLCs and pseudocapacitors simultaneously. Nanostructured electrode materials possess enhanced active electrochemical sites for rapid and stable ionic transport in a relatively short range of diffusion which in turn ensures a good electrochemical response.[12–14] Despite numerous reported attempts of synthesizing mesoporous materials, nanostructured composites and self-assembled micro/nanostructures including nanofilms, nanoparticles, and nanorods,[7,14–16] major problems such as low electrical conductivity and low cycling stability especially at high charge/discharge rates[17,18] persist with the usage of nanostructured materials including various carbon nanostructures such as graphene,[19] carbon nanotubes (CNTs),[20–22] metal oxides[23,24] and chalcogenides such as sulphides,[25–28] selenides[29] and tellurides.[30]

LMDs, in particular, have proven to be one of the primary candidates in this quest for nanostructured electrode materials. This is due to their layered structures in which chalcogenide ions occupy positions hexagonally between octahedrally coordinated metal ions, resulting in distinct layers bound by weak van der Waals (VdW) interactions[31,32] which ensure more space for accumulation of charges. Furthermore, LMDs exhibit metallic phases and multiple oxidation steps which enhance electrical conductivity and specific capacitance, respectively.[25,33] Among them, tin(IV) sulphide (SnS$_2$) has been utilized in a variety of high-performance device applications including but not limited to solar cells, photodetectors, laser diodes, sensors (gas, biomedical, piezoelectrical, and tribological), and energy storage devices (supercapacitors and batteries) owing to its abundance, non-toxicity and eco-friendliness.[34–55] But like other nanostructured materials, problems such as low to moderate ionic conductivity and low stability are also associated with SnS$_2$. Among numerous methods, one simple method of boosting the performance of the SC is doping. Performance enhancement by means of metallic doping has been effective in many other applications such as photocatalysis,[56,57] CO$_2$ reduction,[58] photodiodes[59] and water splitting.[60] In the context of energy storage, attempts have been made by Ma et al. to dope few layered SnS$_2$ nanosheets with molybdenum for SC electrodes,[61] Chen et al. to dope copper in SnSe$_2$ electrodes in LIBs,[62] Asen et al. to synthesize SnS$_2$–SnO$_2$ nano-heterostructures for SC electrodes,[63] Wang et al. to enhance the performance of SnS$_2$ by doping with cobalt for sodium-ion batteries (SIBs),[64] Setayeshmehr et al. to alkali-dope 3D flower-like SnS$_2$ for binder free electrodes in SCs[65] and Wang et al. to synthesize Cu-doped

SnS$_2$ quantum dots anchored on reduced graphene oxide (rGO) for electrodes in SCs[66] which have contributed significantly to the understanding of the subject.

This study presents a straightforward and efficient one-step solid-state method for synthesizing Cu-doped SnS$_2$ nanoflakes and compares their electrochemical behavior to that of pristine SnS$_2$. Since copper is known for its high electrical conductivity, we expected that the copper ions would form substitutional centres where they would enhance local charge transport and facilitate the redox activity on the electrode surface by high adsorption of migrated Al ions.[67,68] The flake-like structures are capable of withstanding volumetric expansion and furthermore, copper and tin ions present have very low difference in their ionic radii which makes lattice distortions less probable.[69] Hence, copper has been chosen as a worthy metallic dopant to serve the purpose of electrochemical enhancement without compromising the stability of the system. The findings are noteworthy, demonstrating a substantial 40% increase in maximum specific capacitance in 5% Cu-doped SnS$_2$ electrodes (140 F g^{-1}) compared to that in pristine SnS$_2$ electrodes (98 F g^{-1}). Importantly, this enhancement in performance is achieved without any alterations in the lattice structure, thereby preserving the stability of the material. These results highlight the potential of Cu-doped SnS$_2$ as a promising electrode material for high-performance aqueous Al-ion SCs. Further exploration into various doping concentrations and their impact on the electrochemical properties of simple materials could yield valuable insights.[68] This research could pave the way for the development of next-generation energy storage devices without the necessity of synthesizing highly advanced composites, creating complex morphologies, generating toxic or hazardous chemical waste, or increasing the carbon footprint.

2 Experimental

2.1 Materials

Copper(II) sulphate pentahydrate (CuSO$_4$·5H$_2$O, 98%) and thiourea (NH$_2$CSNH$_2$, 99%) powders were purchased from Merck. Tin(II) chloride hexahydrate (SnCl$_2$·6H$_2$O, 99%) powder was purchased from Sigma-Aldrich. All reagents were of analytical grade.

2.2 Synthesis of pristine and 5% Cu-doped SnS$_2$

The synthesis route is similar to the process incorporated by Huang et al.[70] as shown in Fig. 1. The preparation of Cu-doped SnS$_2$ nanoflakes was carried out using an ex situ solid state synthesis. First, 2.1437 g (7.2 mmol) of SnCl$_2$·6H$_2$O, 0.1352 g (0.5 mmol) of CuSO$_4$·5H$_2$O and 1.5224 g (0.02 mol) of thiourea
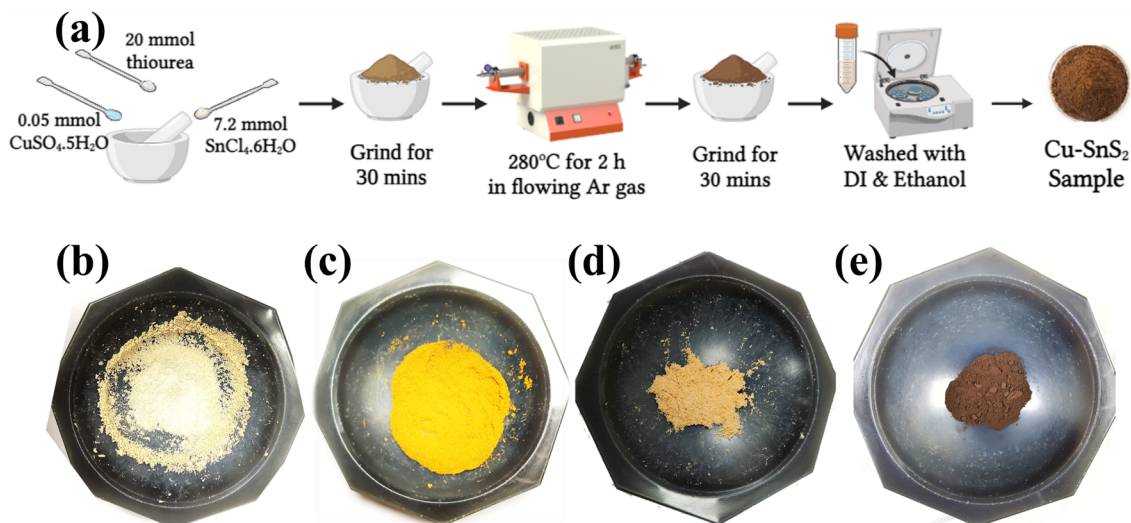
Fig. 1 (a) Schematic illustration of the procedure for synthesizing Cu-doped SnS_2 nanoflakes. (b–e) Comparative images illustrating the visible changes in SnS_2 and Cu-SnS_2 nanoflakes before and after heating in an inert furnace. (b) SnS_2 before heating, (c) SnS_2 after heating, (d) Cu-SnS_2 before heating, and (e) Cu-SnS_2 after heating.

were mixed and ground in an agate mortar for 30 min to make the above mixture homogeneous. Then, the mixture was transferred to an alumina crucible which was placed in a tube furnace. The sample was heated at 280 °C for 2 h in flowing N_2 gas after which the products were allowed to cool to room temperature naturally. An agate mortar was used to grind the powder again. The sample was further washed with DI water and ethanol several times to remove any impurities present. The purified sample was dried at 90 °C for 10 h to obtain the final sample powder. Pristine SnS_2 was prepared using the same procedure barring the addition of $CuSO_4 \cdot 5H_2O$.

2.3 Physiochemical characterization

The crystallographic information of the synthesized materials was extracted by analysis of X-Ray Diffraction (XRD) profiles measured using a Rigaku Miniflex diffractometer with Cu-Kα radiation ($\lambda = 1.5406$ Å) X-ray source. The sample was further investigated by Fourier transform infrared (FTIR) spectra collected using a Shimadzu IR Spirit in transmittance mode (400–4000 cm^{-1}). The morphologies of the synthesized structures were investigated using scanning electron microscopy (SEM Carl Zeiss Supra 40). The elemental mapping data, by energy dispersive X-ray spectroscopy (EDS), were collected using a Carl Zeiss AURIGA OXFORD-XMAXN 50. The N_2 adsorption–desorption isotherms were produced using the Brunauer–Emmett–Teller (BET) technique at 77 K using a Quantachrome NOVA-Touch surface area and pore size analyser. X-ray photoelectron spectroscopy (XPS) spectra were produced using a PHI 5000 Versa Probe III system with a monochromatic Al Kα (1486.7 eV) source. The carbon peak [C–C (sp^3)] was calibrated for charge correction at 284.7 eV.

2.4 Electrochemical characterization

The electrochemical analyses such as cyclic voltammetry (CV) and galvanostatic charge–discharge (GCD) of the synthesized

materials were carried out using a Metrohm Autolab (PGSTAT302N) galvanostat. For determining the material's electrochemical performance, a three-electrode configuration was used in 1 M aq. $AlCl_3$ electrolyte. The three-electrode system was composed of Ag/AgCl (in 3 M KCl) as the reference electrode, a platinum rod as the counter electrode, and an active material coated on a graphite sheet as the working electrode. The working electrode was prepared by mixing 80 wt% (40 mg) active material, 10 wt% (5 mg) activated carbon (as a conductive agent), and 10 wt% (5 mg) polyvinylidene fluoride (PVDF) (as a binder) using acetone as the mixing medium. The mixture was ultrasonicated and then stirred at 60 °C to obtain a homogeneous slurry. The obtained slurry was drop-cast uniformly on a graphite sheet over an area of 1 cm^2 with a typical mass loading of ~1 mg cm^{-2}. Finally, the electrodes were dried under vacuum at 80 °C for 12 h.

3 Results and discussion

3.1 Physiochemical properties

Pristine and 5% Cu-doped SnS_2 nanostructures were synthesized using an *ex situ* solid state technique. Fig. 1 displays the visible difference in the colour of both the samples before and after calcining at 280 °C. The as-synthesized SnS_2 and 5% Cu-doped SnS_2 were subjected to X-ray diffraction (XRD) analysis to investigate their crystallographic properties and phase purity. The obtained XRD pattern, as depicted in Fig. 2(a), was indexed using JCPDS card no. 23-0677. For both samples, distinct peaks were observed around $2\theta = 15, 28, 32, 42$, and 50°, corresponding to the (001), (100), (101), (102), and (111) planes, respectively, which are attributed to the hexagonal phase of SnS_2.§ Analysis revealed

§ The conversion from Miller–Bravais (M–B) indices ($hkil$) to traditional Miller indices (hkl) was done by removing the redundant third M–B coordinate using the relation $i = -(h + k)$.
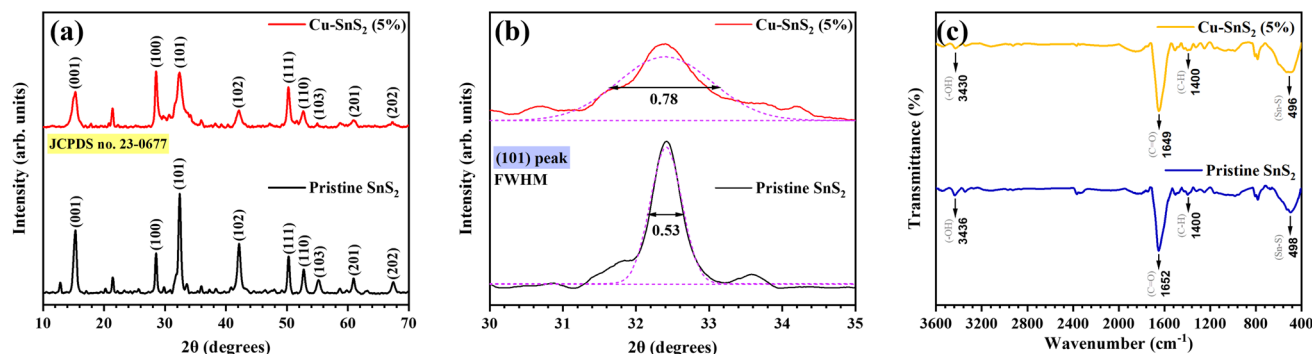
Fig. 2 (a) XRD profiles of pristine and 5% Cu-doped SnS_2 with (b) magnified view of (101) peak broadening. (c) FTIR spectra of pristine and 5% Cu-doped SnS_2.

that the addition of Cu did not introduce any additional peaks beyond those attributed to SnS_2, indicating that the crystal structure of SnS_2 remained unaltered upon doping with Cu. Moreover, minimal peak shifting was observed post-doping, suggesting the absence of significant lattice distortions induced by the incorporation of Cu atoms, as a consequence of the very small difference in ionic radii of parent and dopant atoms.[69] In the pristine SnS_2 sample, the intensity of the (101) peak predominated over others, indicating a preferential orientation of the lattice with crystal growth highly oriented along the basal planes perpendicular to the *c*-axis direction. This observation aligns with the hexagonal crystal structure of SnS_2.[71] Furthermore, broadening of most characteristic peaks was noted in the doped sample, suggesting a reduction in the crystallinity of SnS_2 as a result of local charge disruption due to substitution of copper ions in central cationic sites replacing tin ions. This reduction in crystallinity was particularly evident in the broadening of the (101) peak because of its high density of substitutional sites, as illustrated in Fig. 2(b). The crystallite sizes were quantified using Scherrer's formula, utilizing the most intense (101) peak for both samples whose observations are listed in Table 2 along with their respective lattice parameters. The crystallite size (*D*) was found to decrease from 16.15 nm for pristine SnS_2 to 11.05 nm for Cu-doped SnS_2, indicating an effect of doping on the crystalline domain size.

FTIR spectra of both samples were collected and their examination revealed Sn–S bond formation at 498 cm^{-1} which showed negligible shift after doping as shown in Fig. 2(c). The C–O and C–H bonds were also present as organic constituents such as thiourea were used which dissociates *via* multiple chemical routes at high temperatures and is prone to releasing

carbonyl or ether like compounds.[72] Also –OH had a very low intensity as moisture content was very low due to heating in the inert furnace. Brunauer–Emmett–Teller (BET) theory explained the physical adsorption of gas molecules on a solid surface. In order to calculate pore size, volume, and BET surface area, N_2 adsorption–desorption surface area experiments were performed. The N_2 adsorption–desorption isotherms for the samples were recorded at 77 K and are shown in Fig. 3 with the pore size distributions for the samples given in insets. It has been clearly observed from Fig. 3 that BET isotherms of the synthesized materials are type I isotherms which depict the sole presence of micropores in the samples which indicate that
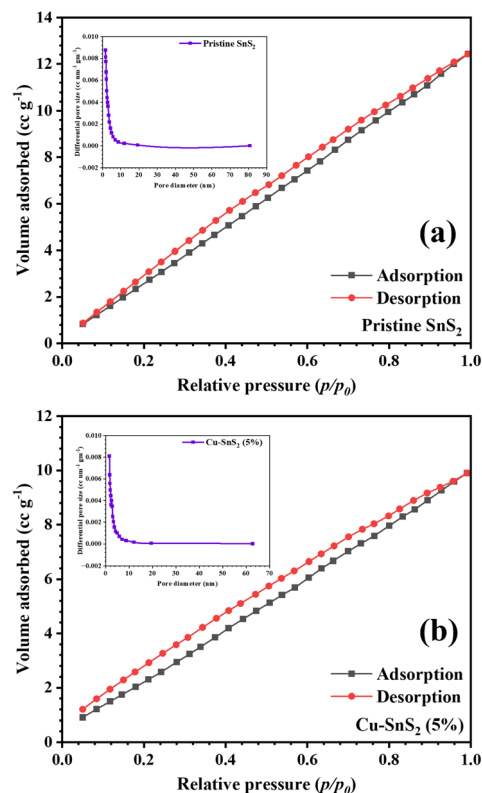
Table 2 Crystallite sizes and lattice parameters corresponding to the most intense (101) peak for pristine and 5% Cu-doped SnS_2 samples

Sample	Peak position 2θ (°)	FWHM β (°)	Crystallite size D (nm)	Lattice constants (Å)	
				$a = b$	c
Pristine SnS_2	32.411	0.535	16.15	3.60	5.90
5% Cu-doped SnS_2	32.364	0.782	11.05	3.61	5.88

Fig. 3 N_2 adsorption–desorption isotherms for (a) pristine and (b) 5% Cu-doped SnS_2 with their respective pore size distributions given in the insets.
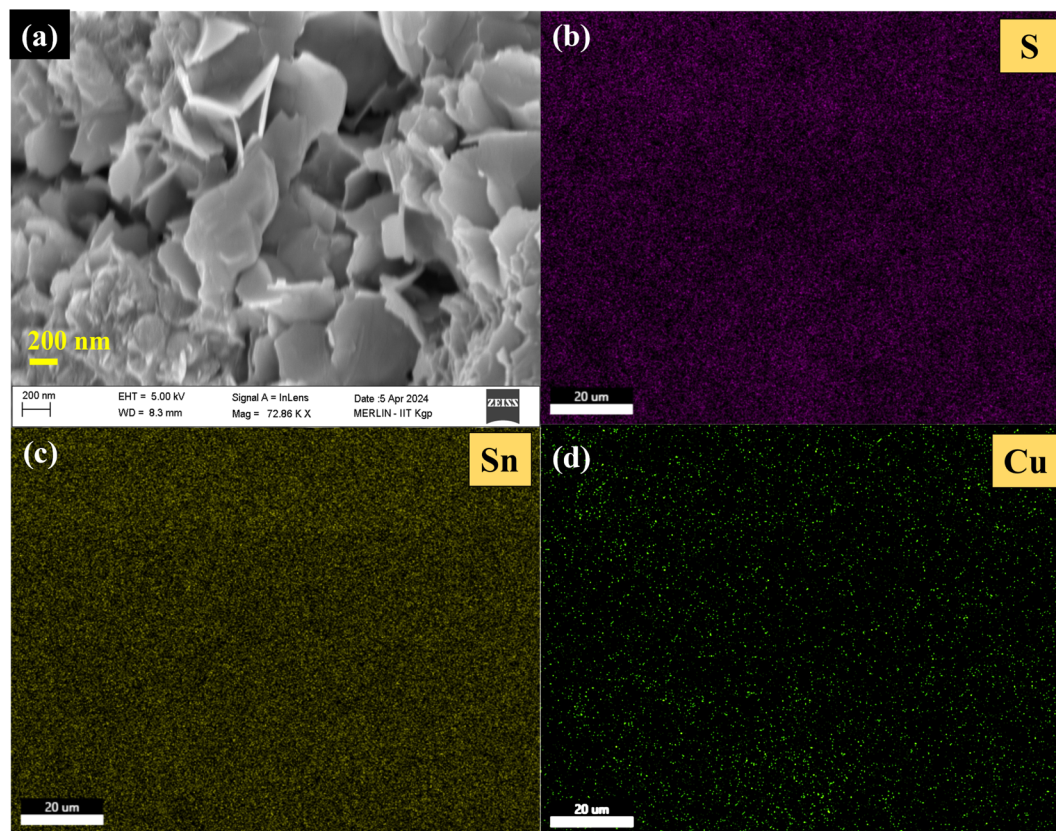
Fig. 4 (a) SEM micrograph showing flake-like morphology of Cu-doped SnS$_2$ nanostructures. (b–d) Elemental mapping for S, Sn and Cu respectively.

materials are microporous with an average pore radius found to be nearly 1.58 nm for both samples. There was minimum hysteresis in the isotherms as there was negligible coalescence of micropores to form larger ones during adsorption which indicates a good mechanical resilience of the sample which is consistent with XRD data as well. The specific surface area was found to be 13 m^2 g^{-1} and 11 m^2 g^{-1} for pristine and Cu-doped SnS$_2$, respectively, indicating the blockage of certain interstitial spots on the surface by neutral copper atoms which was confirmed by the Cu^0 peak in the XPS core spectrum of copper in Fig. 5(b).

Fig. 4(a) shows a highly magnified SEM micrograph of the 5% copper doped sample of SnS$_2$. The image clearly shows that a nanostructure with a flake-like morphology was formed which was in correspondence to the expected results. These results are particularly interesting as these nanoflakes comprise folds which are crucial for compensating volume expansion, thus improving stability and specific capacitance as has been evident

from previous studies.[53,55] Also, the EDS spectrum of the same is reported in Fig. 4(b–d) with the corresponding SEM image given in Fig. S9(a).† The composition of elements is given in Table 3. The EDS spectrum shows a homogeneous distribution of both Sn and S. The presence of Cu was also detected through EDS analysis.

XPS analysis was performed on the Cu-doped SnS$_2$ sample whose results are shown in Fig. 5. The XPS was operated at 15 kV with the carbon 1s signal as the reference peak at a binding energy of 284.7 eV. Fig. 5(a) shows the XPS survey spectrum which confirms the presence of Sn, S and Cu. Also, a carbon peak was observed due to involvement of organic compounds during synthesis. The synthesis protocol was carried out in an inert N$_2$ atmosphere which is responsible for a N 1s peak. Other peaks such as O 1s and Cl 1s are due to the minute formation of SnO$_2$ (due to surface oxidation) and residual SnCl$_2$ of the reaction. Sn 3d peaks were observed at energies ~485 eV (Sn 3d$_{5/2}$) and 494 eV (Sn 3d$_{3/2}$) along with satellite peaks. Similarly, S 2s peaks were found at energies ~160 eV (S 2p$_{3/2}$) and 161 eV (S 2p$_{1/2}$). The confirmation of Cu replacing the central Sn atom and formation of the Cu–S bond was revealed by the stable Cu^{2+} peaks at ~931 and 952 eV which indicated successful doping of Cu in SnS$_2$.

3.2 Electrochemical performance

The electrochemical performance of both undoped and Cu-doped SnS$_2$-based electrodes was systematically investigated in
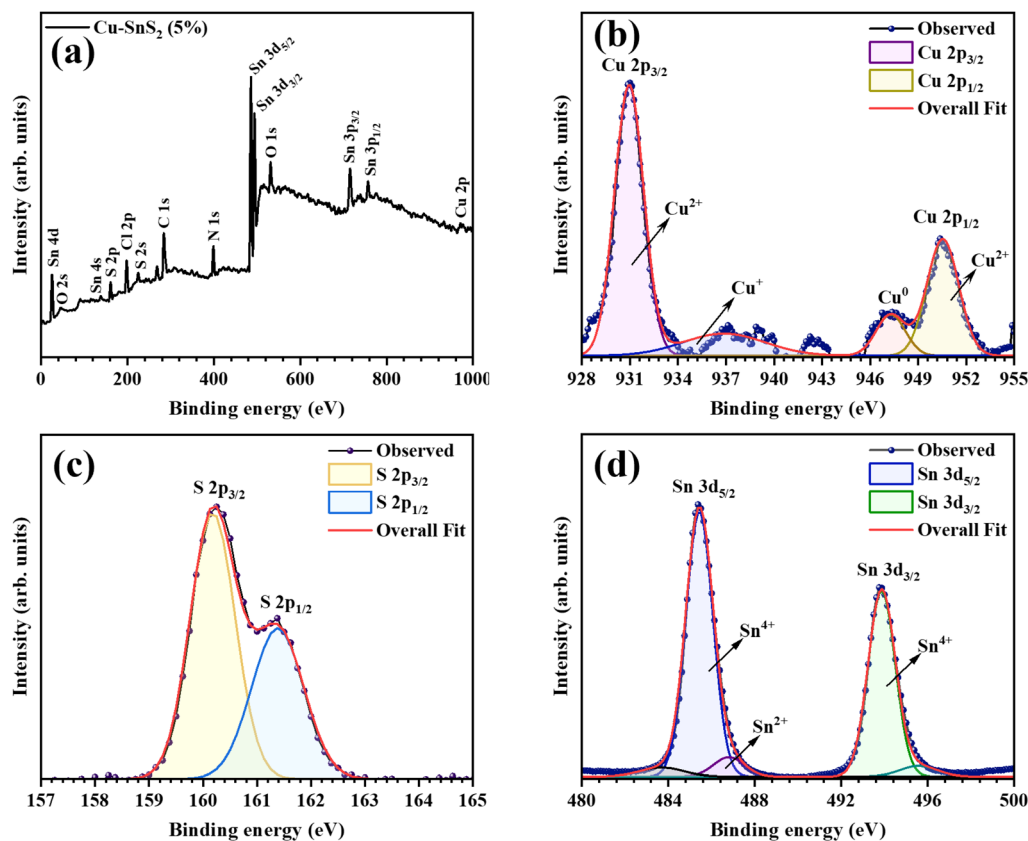
Table 3 Elemental composition for 5% Cu-doped SnS$_2$

Element	Percentage (%) presence in sample
Sn	49
S	48
Cu	3

Fig. 5 (a) XPS survey spectrum for 5% Cu-doped SnS$_2$ and XPS spectra showing peaks for (b) Cu 2p, (c) S 2p and (d) Sn 3d.

a 1 M AlCl$_3$ electrolyte, with the measurements carried out within an optimal potential window ranging from −0.2 V to 1.0 V. Fig. 6(a) and (b) illustrate the cyclic voltammograms (CVs) for the pristine and 5% Cu-doped SnS$_2$ coated electrodes, respectively, recorded at various scan rates ranging from 5 to 200 mV s^{-1}. The CV plots for both samples exhibit a nearly rectangular shape which suggests efficient charge storage through the formation of a double-layer. However, the deviations observed in the CV curves can be attributed to the pseudocapacitive contributions, indicating that faradaic processes are also involved in the energy storage mechanism.

To quantify the specific capacitance of the electrodes, the area under the CV curves was calculated. For the 5% Cu-doped SnS$_2$ sample, the specific capacitance values were found to vary significantly with the scan rate. At a low scan rate of 5 mV s^{-1}, the specific capacitance reached 114 F g^{-1}, demonstrating high charge storage capacity. As the scan rate increased to 200 mV s^{-1}, the specific capacitance decreased to 34 F g^{-1}, which can be attributed to the time limitation for ion diffusion into the electrode material's interior at higher scan rates. Conversely, the pristine SnS$_2$ sample exhibited a specific capacitance of 93 F g^{-1} at 5 mV s^{-1}, which decreased to 27 F g^{-1} at 200 mV s^{-1}, as depicted in Fig. 7(a).

Further electrochemical characterization was conducted using galvanostatic charge–discharge (GCD) measurements, as shown in Fig. 6(c and d). For the pristine SnS$_2$ sample, the GCD analysis revealed a maximum specific capacitance of 98 F g^{-1} at

a current density of 1 A g^{-1}. In comparison, the 5% Cu-doped SnS$_2$ sample demonstrated a significantly higher specific capacitance of 140 F g^{-1} at the same current density, highlighting the superior performance of the Cu-doped SnS$_2$ electrode over the pristine SnS$_2$ electrode, suggesting that the introduction of copper ions improves the electrode's conductivity and charge storage capability, possibly by increasing the number of active sites for faradaic reactions and facilitating better ion transport within the electrode material.

The detailed GCD results, summarized in Fig. 7(b), confirm the enhanced charge storage capacity of the Cu-doped SnS$_2$ electrodes. The GCD profiles for both samples displayed nearly symmetric charge–discharge curves, indicative of good capacitive behavior and high coulombic efficiency. The slight asymmetry is a characteristic of faradaic materials.[9] The Cu-doped sample not only exhibited a higher specific capacitance but also maintained this advantage across various current densities, suggesting improved rate capability and faster ion diffusion kinetics.[13]

Charge–discharge cycling of Cu-doped SnS$_2$ electrodes was conducted at a current density of 3 A g^{-1} to evaluate the long-term stability and durability of the electrode material. The results, as depicted in Fig. 7(c), indicate that the Cu-doped SnS$_2$ electrode exhibits remarkable cycling stability. Initially, the coulombic efficiency was recorded at 93.9% during the first cycle. Impressively, even after 500 charge–discharge cycles, the coulombic efficiency only slightly reduced to 92.7%. This
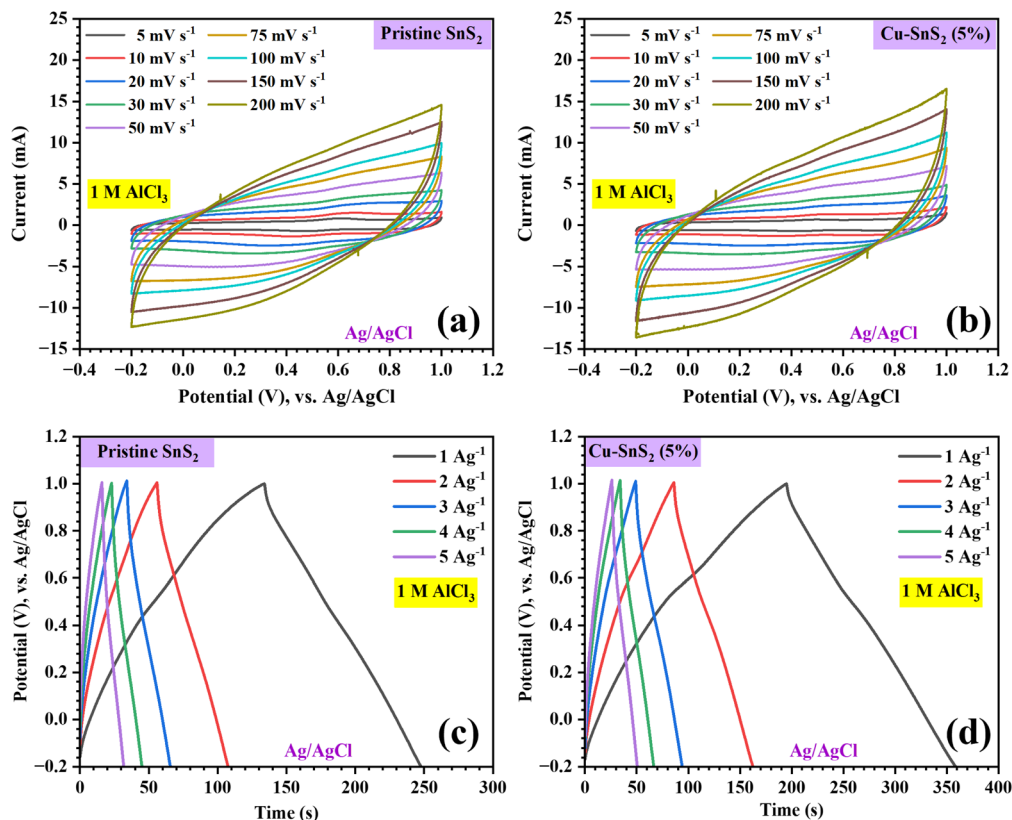
Fig. 6 Cyclic voltammograms for (a) pristine and (b) 5% Cu-doped SnS$_2$ and charge–discharge curves of (c) pristine and (d) 5% Cu-doped SnS$_2$.
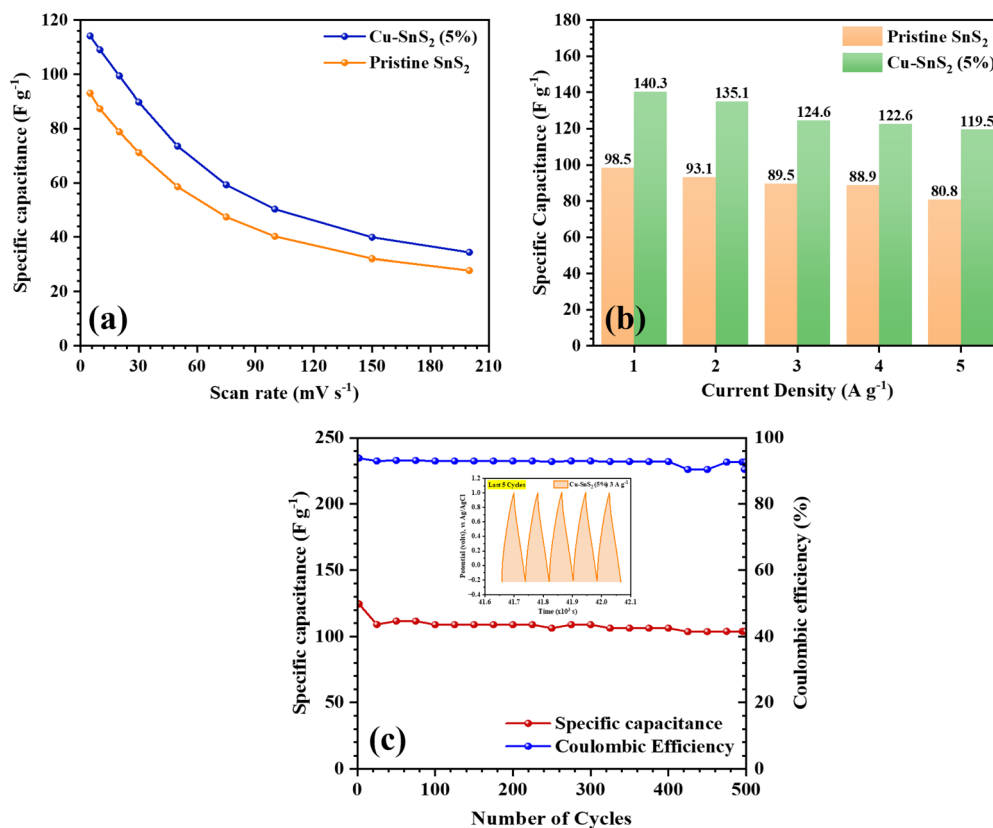

Fig. 7 Variation of specific capacitance with (a) scan rates and (b) current densities. (c) Cycling stability of the 5% Cu-doped SnS$_2$ electrode at 3 A g^{-1} with the last 5 charge–discharge cycles given in the inset.

Table 4 Comparison with previously reported results for SnS_2 based electrodes in SCs

Cathode material	Synthesis method	Electrolyte	Specific capacitance (F g^{-1})	Current density (A g^{-1})	References
SnS_2 nanosheets	Hydrothermal	3.5 M KOH	89.4	1.0	61
SL-SnS_2	Solvothermal	2 M KOH	117.1	1.0	53
SnS_2-SnO_2 (TU)	Hydrothermal	0.5 M Na_2SO_4	71.4	2.0	63
Porous SnS_2	Co-precipitation	1 M Li_2SO_4	123	1.0	55
Li-SnS_2	Solvothermal	0.5 M Na_2SO_4	126	0.1	65
Cs-SnS_2	Solvothermal	0.5 M Na_2SO_4	67	1.0	65
SnS_2/MoS_2	Hydrothermal	1 M KCl	105.7	2.35	71
SnS_2-g-C_3N_4	Solvothermal	3.5 M KOH	178	1.0	73
CF-SnS_2	Solvothermal	1 M KCl	524.5	0.08	74
5% Cu-SnS_2 nanoflakes	Solid-state	1 M $AlCl_3$	140	1.0	This work

minimal decrease of just 1.2% underscores the excellent stability and resilience of the Cu-doped SnS_2 electrode material over extended cycling even in an acidic electrolyte such as $AlCl_3$. In addition to coulombic efficiency, specific capacity retention was also assessed. The specific capacity at the first cycle was considered the benchmark, and throughout the 500 cycles, there was a minor decline in performance. By the end of the 500th cycle, the specific capacity had only decreased by approximately 20%. This demonstrates that Cu-doped SnS_2 maintains a significant portion of its charge storage capability, even after extensive cycling.

The observed performance can be attributed to the beneficial effects of copper doping, which enhances the structural integrity and electrochemical stability of the SnS_2 electrode material. Copper doping introduces additional active sites for redox reactions and improves the electronic conductivity of SnS_2, facilitating better charge transport and storage. These factors contribute to the observed high coulombic efficiency and specific capacity retention over extended cycling.

4 Conclusions

In this work, we introduced a simple and rapid solid-state method for doping SnS_2 nanostructures with copper. The nanostructures exhibited minimal alteration in the lattice structure, porosity, and bonding, as identified by XRD, BET, and FTIR analyses, respectively. SEM images confirmed that 5% Cu-doped SnS_2 exhibited a flake-like morphology, while EDS analysis verified a near-uniform distribution of all elements. The successful doping was further corroborated by XPS analysis, which displayed Cu 2p peaks. The electrochemical performance of the 5% Cu-doped SnS_2 sample was significantly superior to that of the pristine SnS_2 sample in an aqueous $AlCl_3$ electrolyte, demonstrating a remarkable 40% enhancement in maximum specific capacitance. The specific capacitances of the doped sample were consistently higher across all scan rates and current densities, indicating an overall improvement in performance. Furthermore, the coulombic efficiency only decreased by 1.2% after 500 cycles, underscoring the excellent stability of the doped material. These findings suggest that a straightforward doping procedure can achieve substantial performance enhancements without resorting to complex synthesis methods, precisely controlled morphologies, or the creation of composites, nanohybrids, or heterostructures (Table 4). This approach not only advances the development of high-performance energy storage devices but also promotes a more sustainable and environment friendly future by minimizing the use of toxic chemicals and reducing the carbon footprint.

Data availability

The data supporting this article have been included as part of the ESI.†

Author contributions

D. Chatterjee – conceptualization, data curation, visualization, writing – original draft. S. Das – data curation, formal analysis, writing – review & editing.

Conflicts of interest

The authors declare no conflicts of interest.

Acknowledgements

Notes and references

1 K. Brun, T. C. Allison and R. Dennis, *Thermal, Mechanical, and Hybrid Chemical Energy Storage Systems*, Academic Press, 2020.
2 A. K. Rohit, K. P. Devi and S. Rangnekar, *J. Energy Storage*, 2017, **13**, 10–23.
3 U. EIA, *Electricity Explained - Energy Storage for Electricity Generation*, U.S. Energy Information Administration, 2023.

4 B. E. Conway, *Electrochemical Supercapacitors: Scientific Fundamentals and Technological Applications*, Springer Science & Business Media, 2013, pp. 6–7.

5 M. Pathak, D. Bhatt, R. C. Bhatt, B. S. Bohra, G. Tatrari, S. Rana, M. C. Arya and N. G. Sahoo, *Chem. Rec.*, 2024, **24**, e202300236.

6 G. Wang, L. Zhang and J. Zhang, *Chem. Soc. Rev.*, 2012, **41**, 797–828.

7 S. V. Mulik, S. A. Jadhav, P. S. Patil and S. D. Delekar, *Advances in Metal Oxides and Their Composites for Emerging Applications*, Elsevier, 2022, pp. 135–185.

8 P. Sharma and T. Bhatti, *Energy Convers. Manage.*, 2010, **51**, 2901–2912.

9 C. Costentin, T. R. Porter and J.-M. Savéant, *ACS Appl. Mater. Interfaces*, 2017, **9**, 8649–8658.

10 Y. Jiang and J. Liu, *Energy Environ. Mater.*, 2019, **2**, 30–37.

11 M. Kandasamy, S. Sahoo, S. K. Nayak, B. Chakraborty and C. S. Rout, *J. Mater. Chem. A*, 2021, **9**, 17643–17700.

12 A. Nayak, B. Bhushan, S. Kotnala, N. Kukretee, P. Chaudhary, A. R. Tripathy, K. Ghai and S. L. Mudliar, *Mater. Today: Proc.*, 2023, **73**, 227–232.

13 B. Pandit, S. R. Rondiya, S. Shegokar, L. K. Bommineedi, R. W. Cross, N. Y. Dzade and B. R. Sankapal, *Sustainable Energy Fuels*, 2021, **5**, 5001–5012.

14 Z. Yu, L. Tetard, L. Zhai and J. Thomas, *Energy Environ. Sci.*, 2015, **8**, 702–730.

15 R. Liu, J. Duay and S. B. Lee, *Chem. Commun.*, 2011, **47**, 1384–1404.

16 J. H. Fendler, *Chem. Mater.*, 1996, **8**, 1616–1624.

17 X.-Y. Yu, L. Yu, L. Shen, X. Song, H. Chen and X. W. Lou, *Adv. Funct. Mater.*, 2014, **24**, 7440–7446.

18 J. Kang, A. Hirata, H. Qiu, L. Chen, X. Ge, T. Fujita and M. Chen, *Adv. Mater.*, 2013, **26**, 269–272.

19 Q. Cheng, J. Tang, J. Ma, H. Zhang, N. Shinya and L.-C. Qin, *Phys. Chem. Chem. Phys.*, 2011, **13**, 17615–17624.

20 R. A. Fisher, M. R. Watt and W. J. Ready, *ECS J. Solid State Sci. Technol.*, 2013, **2**, M3170.

21 Q. Wang, Y. Li, T. Meng, B. Huang, L. Hu, H. Su, C. Meng and Y. Tong, *ACS Appl. Energy Mater.*, 2021, **4**, 1548–1559.

22 H. Pan, J. Li and Y. Feng, *Nanoscale Res. Lett.*, 2010, **5**, 654–668.

23 V. Sharma, I. Singh and A. Chandra, *Sci. Rep.*, 2018, **8**, 1307.

24 D. Majumdar and S. Ghosh, *J. Energy Storage*, 2021, **34**, 101995.

25 O. Öztürk and E. Gür, *ChemElectroChem*, 2024, e202300575.

26 T. Zhu, Z. He, Z. An, R. Xu, Y. Li, R. Zhe, H.-E. Wang and H. Pang, *Sci. China Mater.*, 2023, **66**, 2216–2226.

27 M. Arif, J. Riaz, A. Bibi, H. Yang and T. Zhu, *APL Mater.*, 2024, **12**, 071119.

28 Y. He, G. Qiu, Z. Qin, Z. Zhang, Y. Chen, X. Pan, Q. Zha, A. Zha, Y. Xu, S. Luo, *et al.*, *J. Power Sources*, 2022, **539**, 231593.

29 G. Tang, J. Liang and W. Wu, *Adv. Funct. Mater.*, 2024, **34**, 2310399.

30 C. Debbarma, S. Radhakrishnan, S. M. Jeong and C. S. Rout, *J. Mater. Chem. A*, 2024, **12**(30), 18674–18704.

31 L. A. Burton, T. J. Whittles, D. Hesp, W. M. Linhart, J. M. Skelton, B. Hou, R. F. Webster, G. O'Dowd, C. Reece, D. Cherns, *et al.*, *J. Mater. Chem. A*, 2016, **4**, 1312–1318.

32 J. Li, J. Shen, Z. Ma and K. Wu, *Sci. Rep.*, 2017, **7**, 8914.

33 L. Wang, X. Zhang, C. Li, X.-Z. Sun, K. Wang, F.-Y. Su, F.-Y. Liu and Y.-W. Ma, *Rare Met.*, 2022, **41**, 2971–2984.

34 R. Lv, J. A. Robinson, R. E. Schaak, D. Sun, Y. Sun, T. E. Mallouk and M. Terrones, *Acc. Chem. Res.*, 2015, **48**, 56–64.

35 M. Haghighi, M. Minbashi, N. Taghavinia, D.-H. Kim, S. M. Mahdavi and A. A. Kordbacheh, *Sol. Energy*, 2018, **167**, 165–171.

36 Y. Rui, T. Li, B. Li, Y. Wang and P. Müller-Buschbaum, *J. Mater. Chem. C*, 2022, **10**, 12392–12401.

37 E. Aslan, D. Kaya, K. Karadağ, U. Harmancı and F. Aslan, *Ceram. Int.*, 2024, **50**, 27626–27634.

38 S. M. Yadav and A. Pandey, *IEEE Trans. Electron Devices*, 2022, **69**, 1889–1893.

39 C. Fan, Y. Li, F. Lu, H.-X. Deng, Z. Wei and J. Li, *RSC Adv.*, 2016, **6**, 422–427.

40 N. Chakraborty, B. Das, A. Roy, P. Dey, B. Das and K. K. Chattopadhyay, *ACS Appl. Opt. Mater.*, 2024, **2**(7), 1454–1465.

41 Z. Shi, X. Sun, J. Xun, W. Xie, L. Zhou, H. Ma, M. Shao, F. Tian and X. Yang, *Microw. Opt. Technol. Lett.*, 2023, **65**, 1415–1420.

42 D. Gu, X. Wang, W. Liu, X. Li, S. Lin, J. Wang, M. N. Rumyantseva, A. M. Gaskov and S. A. Akbar, *Sens. Actuators, B*, 2020, **305**, 127455.

43 L. Shooshtari, N. Rafiefard, M. Barzegar, S. Fardindoost, A. Irajizad and R. Mohammadpour, *ACS Appl. Nano Mater.*, 2022, **5**, 17123–17132.

44 Z. Yang, Y. Ren, Y. Zhang, J. Li, H. Li, X. H. X. Hu and Q. Xu, *Biosens. Bioelectron.*, 2011, **26**, 4337–4341.

45 Y. Wang, L.-M. Vu, T. Lu, C. Xu, Y. Liu, J. Z. Ou and Y. Li, *ACS Appl. Mater. Interfaces*, 2020, **12**, 51662–51668.

46 P.-K. Yang, S.-A. Chou, C.-H. Hsu, R. J. Mathew, K.-H. Chiang, J.-Y. Yang and Y.-T. Chen, *Nano Energy*, 2020, **75**, 104879.

47 D. Gu, W. Liu, J. Wang, J. Yu, J. Zhang, B. Huang, M. N. Rumyantseva and X. Li, *Chemosensors*, 2022, **10**, 165.

48 J.-H. Jang, M. Lee, S. Park, J.-M. Oh, J. K. Park and S.-M. Paek, *J. Mater. Chem. A*, 2023, **11**, 13320–13330.

49 A. Glibo, N. Eshraghi, Y. Surace, A. Mautner, H. Flandorfer and D. M. Cupid, *Electrochim. Acta*, 2023, **441**, 141725.

50 T. Momma, N. Shiraishi, A. Yoshizawa, T. Osaka, A. Gedanken, J. Zhu and L. Sominski, *J. Power Sources*, 2001, **97**, 198–200.

51 Y. Wang, J. Zhou, J. Wu, F. Chen, P. Li, N. Han, W. Huang, Y. Liu, H. Ye, F. Zhao, *et al.*, *J. Mater. Chem. A*, 2017, **5**, 25618–25624.

52 M. Setayeshmehr, M. Haghighi and K. Mirabbaszadeh, *Energy Storage*, 2022, **4**, e295.

53 N. Parveen, S. A. Ansari, H. R. Alamri, M. O. Ansari, Z. Khan and M. H. Cho, *ACS Omega*, 2018, **3**, 1581–1588.

54 M. Sajjad, Y. Khan and W. Lu, *J. Energy Storage*, 2021, **35**, 102336.

55 D. Mandal, J. Halder, P. De, A. Chowdhury, S. Biswas and A. Chandra, *ACS Appl. Energy Mater.*, 2022, **5**, 7735–7747.

56 T. Di, T. Cao, H. Liu, S. Wang and J. Zhang, *Phys. Chem. Chem. Phys.*, 2023, **25**, 5196–5202.

57 Y. Liu, Y. Zhou, X. Zhou, X. Jin, B. Li, J. Liu and G. Chen, *Chem. Eng. J.*, 2021, **407**, 127180.

58 M. Chen, S. Wan, L. Zhong, D. Liu, H. Yang, C. Li, Z. Huang, C. Liu, J. Chen, H. Pan, D.-S. Li, S. Li, Q. Yan and B. Liu, *Angew. Chem., Int. Ed.*, 2021, **60**, 26233–26237.

59 G. M. Kumar, F. Xiao, P. Ilanchezhiyan, S. Yuldashev, A. M. Kumar, H. Cho, D. Lee and T. Kang, *Appl. Surf. Sci.*, 2018, **455**, 446–454.

60 Y. Hu, T. Bo, R. Xu, N. Mu, Y. Liu and W. Zhou, *ACS Appl. Nano Mater.*, 2023, **6**, 19600–19610.

61 L. Ma, L. Xu, X. Zhou, X. Xu and L. Zhang, *RSC Adv.*, 2015, **5**, 105862–105868.

62 H. Chen, Y. Guo, P. Ma, R. Hu, R. Khatoon, Y. Lu, H. Zhu and J. Lu, *J. Electroanal. Chem.*, 2019, **847**, 113205.

63 P. Asen, M. Haghighi, S. Shahrokhian and N. Taghavinia, *J. Alloys Compd.*, 2019, **782**, 38–50.

64 L. Wang, Q. Zhao, Z. Wang, Y. Wu, X. Ma, Y. Zhu and C. Cao, *Nanoscale*, 2020, **12**, 248–255.

65 M. Setayeshmehr, M. Haghighi and K. Mirabbaszadeh, *Electrochim. Acta*, 2021, **376**, 137987.

66 Z. Wang, Y. Chen, L. Yao, C. Zheng and M. Wang, *J. Alloys Compd.*, 2024, **973**, 172906.

67 C. Zhang, H. Zheng, L. Lin, J. Wen, S. Zhang, X. Hu, D. Zhou, B. Sa, L. Wang, J. Lin, *et al.*, *Adv. Energy Mater.*, 2024, 2401324.

68 R. Tao, H. Fu, C. Gao, L. Fan, E. Xie, W. Lyu, J. Zhou and B. Lu, *Adv. Funct. Mater.*, 2023, **33**, 2303072.

69 R. D. Shannon, *Acta Crystallogr., Sect. A*, 1976, **32**, 751–767.

70 X. Huang, J. Chen and F. Xu, *Chem. Phys. Lett.*, 2020, **739**, 137042.

71 L. Wang, Y. Ma, M. Yang and Y. Qi, *Rsc Adv.*, 2015, **5**, 89069–89075.

72 Z. D. Wang, M. Yoshida and B. George, *Comput. Theor. Chem.*, 2013, **1017**, 91–98.

73 S. A. Ansari and M. H. Cho, *Sustainable Energy Fuels*, 2017, **1**, 510–519.

74 R. K. Mishra, G. W. Baek, K. Kim, H.-I. Kwon and S. H. Jin, *Appl. Surf. Sci.*, 2017, **425**, 923–931.